



## Full Text View

[Volume 29, Issue 10 \(October 1999\)](#)

### Journal of Physical Oceanography

Article: pp. 2595–2606 | [Abstract](#) | [PDF \(193K\)](#)

# Observations of the Scale and Occurrence of Breaking Surface Waves

**Johannes R. Gemmrich\***

*Institute of Ocean Sciences, Sidney, British Columbia, and University of Victoria, Victoria, British Columbia, Canada*

**David M. Farmer**

*Institute of Ocean Sciences, Sidney, British Columbia, Canada*

(Manuscript received February 10, 1998, in final form December 8, 1998)

DOI: 10.1175/1520-0485(1999)029<2595:OOTSAO>2.0.CO;2

### ABSTRACT

Breaking of surface waves was monitored with conductivity measurements at wind speeds up to  $18 \text{ m s}^{-1}$ . This method of wave breaking detection is well defined but excludes microbreakers and breaking of very short gravity waves. Observations in both fetch limited and open ocean conditions reveal that wind speed or wave age are insufficient to characterize breaking activity. A scaling of the breaking frequency based on wind energy input is proposed. This scaling collapses the authors' diverse datasets, consistent with energy dissipation being determined primarily by the high frequency tail of the wave spectrum. Breaking waves with significant air entrainment were observed to have wavelengths between  $\sim 0.1$  of the dominant waves and that of the largest wind waves. The median value of the period of breaking waves is approximately half the period of the dominant waves and the mean height of breaking waves is  $\sim 0.7$  times the significant wave height. Less than 10% of observed breaking events resulted in deeply penetrating air entrainment ( $>0.2 \text{ m}$ ), suggesting the predominance of spilling breakers.

### 1. Introduction

Although breaking of surface waves is known to play an important role in upper ocean processes, our knowledge of their distribution and frequency remains limited, especially in the open ocean. The transfer of gases between the atmosphere and ocean is enhanced due to increased near-surface turbulence

#### Table of Contents:

- [Introduction](#)
- [Measurement approach](#)
- [Detection of breaking](#)
- [Time and length scales](#)
- [Mean geometry of a breaking](#)
- [Frequency of wave breaking](#)
- [Conclusions](#)
- [REFERENCES](#)
- [TABLES](#)
- [FIGURES](#)

#### Options:

- [Create Reference](#)
- [Email this Article](#)
- [Add to MyArchive](#)
- [Search AMS Glossary](#)

#### Search CrossRef for:

- [Articles Citing This Article](#)


#### Search Google Scholar for:

- [Johannes R. Gemmrich](#)
- [David M. Farmer](#)

levels and the injection of air bubbles (Thorpe 1982; Kitaigorodskii 1984; Woolf and Thorpe 1991; Farmer et al. 1993; Keeling 1993). Bursting air bubbles generated in the process of wave breaking inject salt and water droplets into the air (Bortkovskii 1987; Ling 1993), contributing to the generation of marine aerosols. At moderate to high wind speed the momentum transfer from wind to ocean currents passes through the wave field via wave breaking (Mitsuyasu 1985; Melville and Rapp 1985; Donelan 1990) and breaking waves are responsible for the dissipation of wave energy (Rapp and Melville 1990; Agrawal et al. 1992), thus being a source of the turbulent kinetic energy of the surface layer.

The ocean surface layer during a storm is a very energetic environment and field observations of wave related processes are challenging. Although new remote sensing techniques are being investigated (Jessup et al. 1997) most of the insight on the dynamics of breaking waves and their contribution to various aspects of air–sea interactions has been gained through controlled laboratory experiments (e.g., Duncan 1981; Rapp and Melville 1990; Jähne 1991; Skyner and Greated, 1992). However, the extent to which laboratory results may be scaled to natural conditions remains open. Key parameters are the frequency of occurrence and scale (length, time, or velocity). Knowledge of the occurrence frequency of breaking waves at a certain point is also of great significance for ocean engineering and risk assessment. However, field observations of breaking frequency exhibit a wide scatter (cf. Thorpe 1993) and observations of the breaking wave scale are sparse (Holthuijsen and Herbers 1986; Ding and Farmer 1994). In this paper we present observations of breaking frequency and scales of breaking waves, obtained with the same instrumentation under various conditions, from a coastal strait to the open ocean. Based on these measurements the scale of breaking waves and mean breaking characteristics are presented and a new scaling of the breaking frequency is proposed.

## 2. Measurement approach

Observations of breaking wave characteristics were obtained during five deployments of a freely drifting instrument described by Farmer and Gemmrich (1996). We monitor breaking wave activity from air entrainment within breaking waves, which is measured by changes in the electrical conductivity of the water (or air–water mixture) at fixed depths. The instrument is equipped with four 4-electrode conductivity cells measuring the effective conductivity within a volume of roughly spherical shape and 0.09-m radius. (Somewhat modified conductivity cells with an effective sampling radius of 0.07 m were used during the deployment in April 1995.) The signal is recorded with a sampling frequency of 34.375 Hz. From this conductivity record an approximate air fraction is then calculated (Lamarre and Melville 1992; Farmer and Gemmrich 1996). In the active part of a breaking wave large amounts of air bubbles are entrained into the top of the water column and the magnitude, duration, and penetration depth of this air entrainment are observed. The instrument was tethered with an  $O$  (30 m) deep drogue, so as to keep the sensors pointing into the wind. The sensor boom has two small surface floats  $\sim 1$  m to each side of the support and is connected via hinged arms to the main instrument housing, containing batteries and a recording system. This floatation keeps the sensors at a nearly constant depth beneath the surface with minimal flow disturbance at the measurement location. Visual observations showed that this design allowed the instrument to ride on the waves without avoiding steep waves or breaking wave crests. The nominal sensor depth of the shallowest sensor was adjusted for different deployments between 0.12 and 0.24 m (Table 1 )

A major challenge lies in maintaining a constant sensor depth even during violent wave breaking. Clearly, this goal can only be reached approximately. Extremely steep waves can occasionally cause the sensor to break through the surface. As discussed by Farmer and Gemmrich (1996) care is taken to detect the distinct signal produced by these events and they are excluded from further analysis. However, it must be recognized that data exclusion for this reason also introduces the possibility that wave breaking events will be missed. In our earlier measurement programs we used a lightweight sensor support supplemented with video recordings. These video recordings showed that the sensor followed the surface closely and also verified the interpretation of low conductivity measurements in terms of high air fractions occurring within breaking waves (Farmer and Gemmrich 1996). A later deployment (18 Apr 1995) supported substantial additional instrumentation, which made the supporting arm heavier. While the additional weight caused the sensor to follow the surface less effectively at wind speeds above  $\sim 14 \text{ m s}^{-1}$ , a capacitance wire gauge was available to track the instantaneous surface elevation relative to the sensors. For wind speed up to  $14 \text{ m s}^{-1}$  fluctuations of the sensor depth are less than 50 mm for 90% of breaking events and our analysis of this particular deployment is limited to this dataset. During four previous experiments a lighter sensor boom followed the surface more precisely and less than 8% of the occurrence of low conductivity measurement resulted from the sensor breaking through the surface.

During the December 1993 and April 1995 experiments the instrument was equipped with flux-gate accelerometers and tilt meters. For these deployments we estimate the surface elevation at the sensor boom from which we calculate the wave height spectrum. The vertical component of the acceleration,

$$a = a_{\text{meas}} / (\cos \Upsilon \cos \Phi), (1)$$

where  $a_{\text{meas}}$  is the measured acceleration and  $\Upsilon$ ,  $\Phi$  are instrument pitch and roll, respectively, is integrated twice in frequency space to obtain the surface elevation. The accelerometers and tilt meters do not give unambiguous separation of

acceleration and tilt and can only provide an estimate of  $a$ . However, for a typical deployment the median absolute pitch is  $<6^\circ$  and the median absolute roll is  $<5^\circ$ , resulting in an uncertainty in the calculation of vertical acceleration of  $\sim 1\%$ . Only about 5% of the time the uncertainty is  $>5\%$ , with a maximum uncertainty of 9%.

Examples of wave measurements and air fraction measurements within breaking events are shown in [Fig. 1](#). The figure also shows the sensor depth beneath the instantaneous surface, measured with the capacitance wire gauge. Conductivity measurements in [Fig. 1a](#) show two peaks. During the strongest event ( $t = 7.3$  s), air fraction reaches a maximum of  $\sim 0.65$  and the sensor stayed at a constant depth of 0.12 m to the free surface. In this example air entrainment at the sensor depth occurs close to, but just after, passage of the wave crest. The height of the breaking wave is 1.9 m and its period is 5.6 s (for definition of wave properties see below). A second smaller conductivity peak appears at  $t = 3$  s. However, during this second event the minimum sensor depth is only 0.06 m, and we therefore attribute the conductivity reduction to the surface proximity of the sensor. If during a breaking event the sensor depth becomes smaller than a limiting value of 0.07 m, we must discard the conductivity signal. The actual sensor depth was in  $\sim 90\%$  of reduced conductivity events greater than 70 mm and in 65% varied by less than 30 mm from the nominal depth of 0.12 m. However,  $\sim 10\%$  of conductivity signals are associated with sensor depths  $<0.07$  m and are not interpreted as breaking events, thereby causing a possible underestimate of the breaking frequency. In the second example ([Fig. 1b](#)) a smaller wave with a height of  $\sim 0.25$  m and period of 2.8 s, riding on a longer wave, is shown. Air fraction reaches a maximum of 0.55 approximately 1 s after the wave crest passed the sensor. However, this does not necessarily imply that air injection occurs on the rear slope of the wave. It is likely that active air entrainment occurred near the crest, but the cloud of air bubbles reaches the sensor depth and is detected only slightly after passage of the wave crest. The sensor depth varied by less than 0.03 m during this breaking event, with a minimum depth of 0.12 m.

The five deployments analyzed in this paper cover a wide range of wind and wave field conditions, which are summarized in [Table 1](#). Standard meteorological observations during the experiments in November 1991 and December 1993 were made with a MiniMet buoy and during the two remaining experiments measurements were made from aboard the research vessel. Buoy wind speed measurements were adjusted from the measuring height of 3 m to a standard height of 10 m according to [Smith \(1981a\)](#). Wind stress estimates were obtained using the bulk aerodynamic method ([Smith 1981b](#)), except for the April 1995 experiment, where the wind stress estimates, based on the eddy correlation method, were kindly provided by J. Edson (WHOI). The wave field was monitored by various means, utilizing either a nearby inverted echo sounder, a wave buoy, or the acceleration of the sensor boom. The dominant wave component is determined from the peak in the wave height spectra and significant wave height is calculated as four times the standard deviation of the surface elevation time series. Comparison between wave parameters obtained from the inverted echo sounder and the sensor boom acceleration is in good agreement. More details of the instrument and deployments are given in [Gemmrich \(1997\)](#).

The first deployment [previously discussed by [Farmer and Gemmrich \(1996\)](#)] took place in the Strait of Georgia in November 1991 ([Table 1](#)). On 24 November 1991 a new wave field developed under a short fetch of  $\sim 20$  km and wind speeds of  $\sim 14$  m s $^{-1}$ . The resulting wave field, monitored with the inverted echo sounder, had a narrow directional spreading and no significant contribution from previous wave fields. The deployment period was eight hours, starting about five hours after the wind speed reached more than 10 m s $^{-1}$ .

On 25 February 1992 our drifter was deployed in the Gulf of Alaska for a duration of 26 hours. The instrument was programmed to record odd hours only. For the first 21 hours the wind speed increased gradually from less than 5 to 17 m s $^{-1}$  and decreased afterwards to a minimum of 6 m s $^{-1}$ , combined with a shift in the wind direction from north to west (see also [Fig. 6](#)). Simultaneous observations of the directional wave field were carried out with a WAVEC buoy by R. Marsden. At the beginning of the drifter deployment the wave field was dominated by the remainder of a storm located to the southeast of the test site, and waves with 0.09 Hz dominant frequency were coming from ESE. Developing wind waves traveled in approximately opposite direction to the swell. At the peak of the storm the wave field consisted of three major spectral components: waves with 0.09 Hz dominant frequency at  $\sim 140^\circ$  and young wave fields with 0.14 Hz and 0.16 Hz dominant frequency at  $\sim 355^\circ$  and  $\sim 15^\circ$ , respectively. A detailed spectral partitioning of the wave field is given by [Hanson \(1996\)](#).

Two further datasets, acquired off the west coast of Vancouver Island in December 1993, include short fetch (3 Dec 1993) and fetch unlimited (9 Dec 1993) conditions at similar wind speeds. Wave height spectra were estimated from the vertical acceleration of the sensor boom ([1](#)). The second deployment (9 Dec 1993) covered the peak of a storm with wind speeds up to 20 m s $^{-1}$ . The low pressure system responsible for this storm, with a center pressure of 952 hPa, was located farther to the north, and a record wave height of 30.8 m was observed in the south entrance of Hecate Strait, just 200 km northwest of the experimental site ([Gower and Jones 1994](#)).

A slightly modified version of the instrument was deployed on 18 Apr 1995 off Monterey, California, as part of the Marine Boundary Layer Program. The emphasis of this deployment was to study turbulence and thermal structure of the near-surface layer ([Gemmrich and Farmer 1999](#)). During the first three hours of the deployment wind speed increased from 10 to

$14 \text{ m s}^{-1}$  and wind waves were rapidly developing, resulting in an increase of the significant wave height from 3 to 3.8 m. In addition to the estimation of the surface elevation according to (1), a sonar system provided directional information of the wave field (Trevorrow and Booth 1995). This showed that developing wind waves and swell were aligned within  $20^\circ$ .

### 3. Detection of breaking waves

The intercomparison of breaking wave field observations are made difficult by the lack of a well-accepted criterion for what constitutes a breaking event. Different measurement techniques rely on varying criteria with somewhat arbitrary thresholds. Breaking wave criteria can be divided into two classes, the first relating to some characteristics of the surface elevation at a point (Longuet-Higgins and Smith 1983; Thorpe and Humphries 1980; Weissman et al. 1984; Katsaros and Ataturk 1992) and the second to observations of air entrainment (Toba et al. 1971; Holthuijsen and Herbers 1986), whitecaps (Monahan and O’Muirhearataigh 1986), or ambient noise (Farmer and Vagle 1988; Ding and Farmer 1994).

Similar to Su and Cartmill (1992) and Lamarre and Melville (1992) we define a breaking event by decreased electrical conductivity caused by air entrainment into the top of the water column. While this criterion utilizes a well-defined measurable property of all breaking waves except microbreaking, the definition of a suitable threshold again seems arbitrary and depends on the precise depth of measurement as well as other factors that we cannot control, such as the vertical gradient of air fraction. We convert the conductivity change into the fraction of air in the water–air mixture. Available theory relating conductivity to air fraction breaks down for large values ( $>0.5$ ) (Olsen 1967). However, for small values we could verify the sensor response in a calibration tank where air fractions up to 0.25 could be realized. Longuet-Higgins and Turner (1974) modeled a spilling breaker as a turbulent gravity current entraining air while riding down the slope of a wave. Their theory predicts that a density difference greater than 8% is required to sustain a steady motion. We therefore define a breaking event as an incident in which the air fraction exceeds 0.08 at our top sensor. However, we find variation of the threshold between 0.05 and 0.1 alters the number of detected breaking events by less than 4%. For much smaller thresholds ( $<0.03$ ) a significantly larger number of events is identified, presumably due to persistent high bubble densities, but possibly not directly related to active breaking. It must also be noted that due to the minimum sensor depth, which is required to prevent apparent air fractions caused by surface proximity, the breaking of very short gravity or capillary–gravity waves is not included in our observations.

### 4. Time and length scales of breaking waves

In the ocean, the scales of breaking waves may cover a very wide range from the microscale of a few centimeters up to the length of the dominant waves. Little is known about the distribution of scales. Phillips (1985) suggested the use of the phase speed  $c_{\text{brk}}$  of the breaking wave together with the dispersion relation defining its scale. Ding and Farmer (1994) tracked the sound of breaking waves in the open ocean and obtained statistics on duration, velocity, spacing, and breaking probability from 23 datasets of 30-min length each. They find the ratio of the phase speed of the breaking wave  $c_{\text{brk}}$  and the phase speed of the dominant waves  $c_p$  to decrease from  $c_{\text{brk}}/c_p = 0.75$  for  $c_p = 4.0 \text{ m s}^{-1}$  to  $c_{\text{brk}}/c_p = 0.45$  for a more developed wave field with  $c_p > 10 \text{ m s}^{-1}$ . Two recent studies, estimating the energy dissipation by breaking waves, also yield a scale of breaking waves. Thorpe (1993) scaled laboratory measurements of dissipation rates of steady breaking waves with observed breaking frequencies and found the energy loss from the waves due to breaking varied as  $E_W \propto \rho_w u^3 (c_{\text{brk}}/c_p)^5$ , where  $\rho_w$ ,  $u$  are water density and wind speed, respectively. To fit the estimated dissipation to observed oceanic dissipation rates,  $c_{\text{brk}}/c_p = 0.25$  is implied. However, as discussed below, this parameterization of the breaking frequency is not supported by our observations. Melville (1994) pointed out that in the more realistic case of unsteady spilling breakers and a more complete account of the oceanic dissipation rate Thorpe’s (1993) model requires  $c_{\text{brk}}/c_p$  to vary between 0.4 and 0.63.

Our measurements combine detection of wave breaking with an estimate of the local surface elevation and therefore allow estimation of the scale of breaking waves. As a first approximation a wave field is characterized by the period of the peak of the wave spectrum  $\tau_p$  and the significant wave height  $H_s$ . We calculated both parameters from surface elevation segments of 30 min duration. For practical purposes, we define individual waves as the period between two successive local minima in the surface elevation, that is, the period between consecutive zero–up crossings of the derivative of the surface elevation, but disregard waves with an elevation change of less than 0.1 m. This exclusion of small surface elevation changes mainly reflects the uncertainty of the surface elevation estimation due to local differences of the wave field at the two sensor boom floats. The threshold of 0.1 m is an estimated upper limit of this uncertainty. For each breaking wave we determine the period of the breaking wave  $\tau_{\text{brk}}$  and the height of the breaking wave  $H_{\text{brk}}$ , which is defined as the difference in the surface elevation between the local minimum prior to the breaking event and the maximum within the period of the breaking wave (see Fig. 1). The definition of individual waves based on zero-crossings of the elevation derivative, rather than zero-crossings of the elevation itself, has the advantage of identifying smaller waves riding on longer waves and is therefore



applied for estimating breaking wave properties. Calculations of the significant wave height and dominant wave period are based on zero crossings of the surface elevation and for broad spectra the two definitions of what constitutes an individual wave lead to different statistical properties. However, by eliminating small amplitude waves the differences are minimized ([Cartwright and Longuet-Higgins 1956](#)).

The following analysis of the scale and geometry of breaking waves is based on 132 breaking events during deployment III as defined as incidents with air fractions  $\geq 0.08$  and a temporal separation to the preceding event of  $\geq 16$  s. This cut-off criterion of a minimum separation between breaking events is required for the subsequent ensemble average and excludes less than 10% of breaking events from the following analysis. To compare our estimate of the scale of breaking waves with literature results we normalize the breaking wave period by the period of the dominant waves and use the dispersion relation for linear deep water gravity waves to obtain  $c_{\text{brk}}/c_p = \tau_{\text{brk}}/\tau_p$ .

Our measurements show that breaking waves exist over a wide range of scales, most of them being significantly shorter than the dominant waves ([Fig. 2](#)). The median value is 0.54. This distribution is based on breaking waves that generate significant air entrainment ( $>0.08$ ) and to wave amplitudes  $>0.1$  m, thus excluding short gravity and capillary-gravity waves. Seventy-seven percent of the data fall within the range 0.2 to 0.8 and only 5% are less than 0.2. [Melville's \(1994\)](#) estimate of  $0.4 < c_{\text{brk}}/c_p < 0.63$  covers only 33% of our data, and the range 0.45 to 0.75 reported by [Ding and Farmer \(1994\)](#) includes 40% of this dataset. [Thorpe's \(1993\)](#) estimate  $c_{\text{brk}}/c_p = 0.25$ , which is partially based on breaking frequencies in coastal waters, is low for this dataset. In terms of wavelength, which is related quadratically to wave phase speed, our data indicate that breaking occurs over a wide range of scales, predominantly between 5% and 80% of the wavelength of the waves containing most energy. For the open ocean this implies that breaking waves with air entrainment can have a length of several meters up to more than 100 m, spanning the full range of wind waves.

The distribution of the normalized surface height at the onset of air entrainment, that is, the point at which the air fraction surpasses a threshold of 0.08, and the normalized height of the breaking wave are shown in [Fig. 3](#). The normalization is carried out with respect to the significant wave height. More than 86% of the observed breaking events show the onset of air entrainment at the sensor depth at a positive elevation above the mean surface level. The median value is at 0.28. For the majority of breaking events the difference in surface elevation between the onset of breaking and the onset of air entrainment at the shallowest sensor depth is insignificant. [Phillips and Banner \(1974\)](#) argue that the augmentation of the surface drift near the long-wave crests facilitates the onset of breaking. Our dataset shows less than 5% of the breaking waves start at surface elevations comparable to the significant wave height and, even if we allow for a 1-s separation between the onset of breaking (which we cannot resolve with our instrumentation) and the onset of air entrainment at the shallowest sensor depth, our data do not support the concept of preferential breaking on or near the crests of longer waves. This, of course, does not preclude preferential breaking of waves smaller than we can resolve with our sensor. The height of breaking waves  $H_{\text{brk}}$  is in 78% of our observations smaller than the significant wave height. The distribution of the normalized height of breaking waves shows a slight peak in the range 0.6–0.9. The median value is 0.66.

## 5. Mean geometry of a breaking wave

Each breaking wave is individual in its characteristics, depending on very local conditions of wave and wind field. However, we expect an inherent mean geometry underlying individual breaking. Therefore we extract all 132 breaking events as data segments of 16-s length and center them at the time when the air fraction exceeds the threshold of 0.08. Subsequently, air fraction and surface height were ensemble averaged ([Fig. 4](#)).

The average air fraction reaches a maximum value of 0.2 and a signal higher than 0.08 lasts for  $\sim 0.3$  s. However, in several cases the signal is up to 1.5 s long, causing the average signal to stay above 0.005 for the duration of these few longer events. The average air fraction rises within  $\sim 0.2$  s from the detection threshold of 0.005 to 0.02 from where it reaches the maximum value within less than 0.2 s. The decrease of the signal is similarly rapid.

As discussed above, the surface elevation of breaking events covers a wide range. Therefore, in each case we reference surface elevation to the minimum value within the breaking wave prior to averaging the surface elevations. Although [Fig. 4](#) shows time series of the air fraction and surface elevation at a fixed point, the graph could also be interpreted as a snapshot of a wave traveling from right to left, shortly after wave breaking occurred.

The surface rises steadily from an average value of 1.1 to 3.4 m within 3.5 s and then decreases to 1.6 m within the following 4 s. The onset of detectable air entrainment at our measurement depth of 0.18 m occurs close to, but slightly after, the mean surface elevation maximum obtained from all breaking waves. The maximum air fraction occurs at a surface elevation 0.17 m below the maximum. In [Fig. 5a](#) the surface elevation of each breaking wave is normalized by its wave height and the time scale by its wave period, leading to a mean normalized surface elevation. The distribution of times of maximum air fraction, scaled with the period of the breaking wave, is shown in [Fig. 5b](#). Combined with the mean surface geometry it illustrates the phase distribution of air entrainment. At 0.18 m below the instantaneous surface a cloud of


air is detected substantially downstream from the crest. This is in accordance with the conceptual model of the active air entrainment occurring predominantly at the crest, where the water particle speed exceeds the phase speed of the wave and spills forward. A similar delay of  $\sim 0.2$  wave periods between the air fraction signal at  $<0.15$  m below the surface and the maximum surface elevation was described for a single example with  $\sim 0.7$  m wave height by [Lamarre and Melville \(1994\)](#) in a study of large-scale three-dimensional laboratory waves.

Our conductivity measurements were made at four depths. The nominal depth of the second sensor was during all deployments greater than 0.25 m. Although we cannot attribute deep entrainment events unambiguously to plunging breakers, laboratory experiments ([Rapp and Melville 1990](#)) support this distinction. [Rapp and Melville \(1990\)](#) find the aerated region in spilling breaking waves resembles a turbulent gravity current, as modeled by [Longuet-Higgins and Turner \(1974\)](#), and is thus confined to a shallow depth. Plunging breaking waves, however, generate much deeper air entrainment ([Rapp and Melville 1990](#)). Our data show a sharp discontinuity in air entrainment at  $\sim 0.2$  m, consistent with the model of a spilling breaking wave, whereas plunging breaking waves of different strengths would generate a continuous distribution of air penetration depths. We hypothesize that large air fractions at depth  $>0.25$  m are associated with plunging breakers. In the open ocean typically less than 2% of breaking events are detectable below this depth. However, during two deployments a much higher fraction of breaking events with deeper air entrainment was found. In Georgia Strait (I) more than 8% of the waves can be detected at depth 0.32 m and 5% at 0.51 m. Within this fetch limited environment the dominant wavelength is roughly one third of typical open ocean waves for comparable wind speeds, but the significant wave height is approximately half the height of waves in fetch unlimited conditions. Hence, these waves are steeper and more likely to plunge down the forward face than open ocean waves. During deployment II 9.5% of breaking events cause detectable air entrainment at 0.46 m and 2% at 0.75-m depth. This high incidence of deeply penetrating air entrainment is most likely linked to the condition of strongly forced wind waves opposing swell, which will also steepen the waves.


## 6. Frequency of wave breaking


The breaking frequency  $f_{\text{brk}}$  is defined as the number of breaking events at a single point per unit time. Data from several field studies have been used to determine the breaking frequency, using various detection methods discussed above ([Toba et al. 1971](#); [Thorpe and Humphries 1980](#); [Longuet-Higgins and Smith 1983](#); [Weissman et al. 1984](#); [Holthuijsen and Herbers 1986](#); [Su and Cartmill 1992](#); [Katsaros and Atatürk 1992](#); [Ding and Farmer 1994](#)). There appears to be no consistent description of the relation between breaking frequency and the relevant physical parameters. This is partly due to the different breaking criteria applied but is also a consequence of incomplete accounts of the physical processes leading to wave breaking.

As a first approximation, the frequency of breaking is expected to follow closely the wind speed. However, a scatterplot of breaking frequency versus wind speed summarizing most of the published data (cf. [Holthuijsen and Herbers 1986](#)) does not collapse diverse datasets, indicating that this description is incomplete. It should also be noted that these measurements were acquired using several different wave breaking detection approaches that could also contribute to the scatter.

For the first 21 hours of deployment II the breaking frequency  $f_{\text{brk}}$  measured by the conductivity sensor at 0.24 m increased from 0.5 to 2.5 breaking waves per minute, as the wind speed increased from 5 to 17  $\text{m s}^{-1}$  ([Fig. 6](#) ). We attribute high air fraction ( $>0.05$  at 0.46 m,  $>0.03$  at 0.75 m) to plunging waves (see discussion above). A surprising observation is that the measured breaking frequency continues to increase after 2020 UTC, although the wind speed decreases. This continues until 0000 26 February 1992, by which time the wind speed had dropped from 17 to 7  $\text{m s}^{-1}$ .

We restrict the following analysis of breaking frequencies to our own data obtained with the same measuring technique in order to minimize possible uncertainties resulting from different wave breaking criteria. Breaking frequencies are averaged within 30-min segments and normalization of the breaking frequency  $f_{\text{brk}}$  by the period of the dominant waves  $\tau_p$  yields the *relative breaking frequency*,  $f_r = f_{\text{brk}} \tau_p$ .

The relative breaking frequency as a function of wind speed ([Fig. 7](#) ) exhibits a wide scatter, despite restricting the analysis to a single detection method for wave breaking. At  $u_{10} \sim 13 \text{ m s}^{-1}$  wave breaking may occur on average at intervals ranging from  $\sim 1.5$  to  $\sim 20$  times the dominant wave period. A general weak trend of higher breaking frequencies at higher wind speed yields a linear regression coefficient,  $r = 0.46$ . [Holthuijsen and Herbers \(1986\)](#) found a much clearer dependence of breaking frequency on wind speed if the analysis is restricted to data obtained by a single observation technique [i.e., measurements by [Toba et al. \(1971\)](#) and [Holthuijsen and Herbers \(1986\)](#)]. Their data were collected in coastal water without noticeable swell and wind wave alignment within  $40^\circ$ . We attribute the poor correlation obtained in this study to complex wave fields and unsteady winds.

During the period of decreasing wind speed in II the significant wave height was still growing until  $\sim 2$  h after the peak wind speed and thus exhibits a similar behavior like the breaking frequency ([Fig. 6](#) ). Evidently the stage of wave

development is a relevant factor in evaluating the breaking frequency. Commonly, the stage of wave development is described by wave age  $c_p/u_{10}$  or  $c_p/u_{*a}$ , where  $c_p$  is the phase speed of the dominant waves,  $u_{10}$  is the wind speed at 10 m height, and  $u_{*a}$  the friction velocity in air. Here we apply the wave age definition based on friction velocity. The relative breaking frequency as a function of inverse wave age exhibits a wide scatter (Fig. 8) and shows no improvement compared to the dependence of relative breaking frequency and wind speed. For individual datasets the relative breaking frequency tends to decrease as the wave field develops. However, no trend holds for different deployments. A commonly assumed linear relationship yields a correlation coefficient  $r = 0.12$ . During III the inverse wave age  $u_{*a}/c_p$  ranges between 0.2 and 0.35 and  $f_r < 0.15$ . For the same range of inverse wave age the relative breaking frequency is two to five times larger during IV. Both datasets were acquired at approximately the same location by the same instrument and the same breaking criterion was applied. Wind speeds for both periods are comparable, but wind direction differs by  $\sim 150^\circ$ , creating a fetch limited environment in III. Fetch during deployment I was even shorter, and these data build a cluster on the scatterplot, almost completely separated from the open ocean data. This separation of individual datasets suggests that wave age is an incomplete descriptor of the conditions associated with wave breaking and the period of dominant waves is not the appropriate normalization of breaking frequency. This is in keeping with the broad range of breaking scales discussed above (Fig. 2), with less than 10% of breaking waves having a scale comparable to the dominant waves.

#### a. Scaling of breaking frequency based on air–sea energy flux

Breaking is believed to be the main factor in wave energy dissipation (Komen et al. 1994). We therefore expect the occurrence of breaking waves, and hence the breaking frequency, to be related to the flux of energy into the wave field, which ultimately determines dissipation. The rate of energy input from the wind into wave components with phase speed  $c$  is

$$F = \tau_w c. \quad (2)$$

The momentum transfer from wind to waves  $\tau_w$  is defined by the wave field momentum transfer function  $G_w(\omega)$ ,

$$\tau_w = \int_0^\infty G_w(\omega) d\omega. \quad (3)$$

Integration over all frequencies and assuming fully rough flow where all air–sea momentum transfer is supported by surface waves (Kinsman 1965; Donelan 1990) yields

$$F_t = \bar{c}_p u_{*a}^2, \quad (4)$$

where  $u_{*a}$  is the friction velocity in water and  $\bar{c}_p$  is the *effective* phase speed of waves acquiring energy from the wind (Gemmrich et al. 1994; Terray et al. 1996), defined as

$$\bar{c}_p = \frac{\int G(\omega) c(\omega) d\omega}{\int G(\omega) d\omega}. \quad (5)$$

Gemmrich et al. (1994) estimated this effective phase speed utilizing measured dissipation profiles from three different investigators with the assumption of a balance between energy input and energy dissipation. Surprisingly, this basic model yielded for all three datasets  $\bar{c}_p = O(0.7 \text{ m s}^{-1})$ ; that is, the air–sea energy input occurs predominantly through form drag of high frequency waves. For fully developed seas, where the balance between energy input and energy dissipation applies, the energy flux can be estimated by (4). This estimate of the energy input with  $\bar{c}_p = 0.7 \text{ m s}^{-1}$  serves as a reference state; however, depending on wind and wave field the exact value of  $\bar{c}_p$  may vary (Terray et al. 1996). Form drag exerted by the wind on a wave component also depends on the amplitude of that wave component, and the energy input  $F_w$  depends on the actual spectrum of the waves:

where  $g$  is the gravitational acceleration,  $S = S(\omega, \Psi)$  is the directional wave height spectrum, and  $\beta$  is the wave growth factor (Plant 1982). Only in the absence of wave–wave interactions, dissipation, and flux divergence of wave energy would  $\beta$  imply a true growth of the wave field and it is more appropriate to interpret  $\beta$  as a coupling function between the wind and wave field. There is general agreement that  $\beta$  is proportional to the square of the wind speed and the cube of the frequency, which reflects the bias of effective energy input towards high frequency waves. However, individual parameterizations for  $\beta$  differ in their exact formulation (Plant 1982; Donelan and Pierson 1987; Hsiao and Shemdin 1983; Caudal 1993). The subsequent calculation of  $F_w$  follows Terray et al. (1996).

Donelan and Pierson's (1987) formulation for  $\beta$ ,

$$\frac{\beta}{\omega} = 0.194 \frac{\rho_a}{\rho_w} \left( \frac{u_{\pi/k} \cos \varphi}{c(k)} - 1 \right) \left| \frac{u_{\pi/k} \cos \varphi}{c(k)} - 1 \right|, \quad (7)$$

offers the weakest coupling between wind and low frequency waves and for a mature wave field approaches the energy input of the reference state. For each wavenumber  $k$ , the term  $c(k)$  represents the phase speed of that component. Wind speed  $u_{\pi/k}$  and wind direction  $\Psi$  relative to wave propagation are evaluated at a reference height corresponding to half the wavelength of this component, assuming a logarithmic wind profile and roughness length  $z_0$  given by Donelan (1990),

$$z_0 = 1.38 \times 10^{-4} H_s \left( \frac{u_{10}}{c_p} \right)^{8/3}. \quad (8)$$

No directional observations of the wave field were obtained in deployments I, III, and IV (see Table 1). A directional spreading of  $\cosh^{-2}(\alpha\Psi)$  (Donelan et al. 1985), where  $\alpha$  is a constant, is assumed for these wave spectra. At frequencies above  $\sim 0.8$  Hz the measured wave spectra become unreliable and a  $\omega^{-5}$  tail (Banner 1990) is added to the spectra from 0.6 to 7.5 Hz. The resulting wind–wave coupling function  $\beta$  is monotonically increasing with frequency  $\omega$ . For conditions during deployment IV no energy input occurs for  $\omega < \sim 2\omega_{pk}$ , where  $\omega_{pk}$  is the frequency of the dominant waves. At the frequency corresponding to  $\bar{c}_p$  the value of  $\beta$  is  $\sim 3 \times 10^{-1} \text{ s}^{-1}$ , or  $\sim 5$  orders of magnitude larger than  $\beta(2\omega_{pk})$ . A maximum of  $\beta = 3 \text{ s}^{-1}$  is reached at our high frequency cutoff. Combined with the surface height spectrum  $S$  this yields a maximum of the wind wave energy input at  $\sim 5\omega_{pk}$ , and therefore at somewhat lower frequencies than implied by (5).

We now define the dependent parameter in the description of the breaking frequency as the energy input into the wave field  $F_w$  (6) normalized by the energy input into a mature wave field  $F_t$  (4):

$$\bar{F} = \frac{F_w}{F_t} = \frac{g \int \beta S d\omega d\varphi}{u_*^2 \bar{c}_p}. \quad (9)$$

This parameter depends mainly on wave components short compared to the peak of the wave spectrum.

Similarly, normalization of the breaking frequency incorporates the timescale of breaking waves rather than the dominant wave period. The scale of breaking waves varies over a wide range (Fig. 2) and might depend on the wave field itself (Ding and Farmer 1994). Kitaigorodskii (1983) proposed the existence of a dissipative subrange at wavenumbers larger than a transitional value

$$k_g = C \frac{g}{E_0^{2/3}}, \quad (10)$$

where  $E_0$  is the energy flux from the region of energy input towards high wavenumbers. Assuming a balance between energy input and dissipation (Gemrich et al. 1994),  $E_0 = F_w$ , the period of waves at the transition to the dissipative



subrange can be estimated as

$$\tau_{\text{diss}} = C^{-1/2} \frac{2\pi F_W^{1/3}}{g}. \quad (11)$$

The constant  $C$  is derived by matching for deployment III dissipation timescales  $\tau_{\text{diss}}$  calculated from (11) and observed periods of breaking waves  $\tau_{\text{brk}}$  (Fig. 2  $\bullet$ ), yielding  $C = (1 \pm 0.24) \times 10^{-4}$ , where the error bounds describe one standard deviation. The timescale  $\tau_{\text{diss}}$ , which can also be obtained on purely dimensional grounds, is related to the breaking wave period and is used to normalize the breaking frequency:

$$\tilde{f}_b = f_{\text{brk}} \tau_{\text{diss}}. \quad (12)$$

The functional dependence between the normalized breaking frequency  $\tilde{f}_b$  and normalized wave energy input  $\tilde{F}$  seems to collapse all four datasets (Fig. 9  $\bullet$ ). Compared to the broad scatter in Fig. 8  $\bullet$  a much more pronounced relationship between the breaking frequency and the forcing parameter emerges. For  $\tilde{F} < 1$  energy input into the local wave field occurs predominantly by advection, as is the case during the beginning of deployment II and during a brief period of decreased wind speed during deployment I. Under these conditions little breaking activity takes place and  $\tilde{f}_b < 0.05$ . When there is excess energy input (i.e.,  $F_W > F_t$ ), breaking waves occur more frequently and  $\tilde{f}_b$  increases roughly linearly. For  $\tilde{F} \geq 1$  the linear correlation coefficient between  $\tilde{f}_b$  and  $\tilde{F}$  is  $r = 0.87$ . The most frequent breaking occurs during deployment IV. The energy input reaches three times the energy input of the reference state described by  $F_t$  and  $\sim 40\%$  of the waves with periods comparable to the mean period of breaking waves are breaking.

The calculation of  $F_W$  (and hence  $\tau_{\text{diss}}$ ) is based on several empirical relationships which might not be generally applicable. However, our datasets span diverse conditions from a coastal strait to open ocean, with great differences in fetch, and although there is some scatter in the result shown in Fig. 9  $\bullet$ , the data appear to collapse under the proposed scaling  $\tilde{f}_b = \tilde{f}_b(\tilde{F})$ . We therefore conclude that surface wave breaking is directly governed by the interaction of wind and high frequency waves, described by the ratio  $F_W/F_t$ . It is not sufficient to characterize the wave field by a single wave component as implied by the use of wave age. An effective breaking wave period  $\tau_{\text{diss}}$  (11) related to this interaction incorporates the whole wave spectrum, subject to a high frequency weighting, and provides an appropriate normalization of the frequency of occurrence of breaking waves.

## 7. Conclusions

Generation of turbulence depends on the strength, scale, and frequency of breaking events. Conductivity measurements in the upper 0.25 m of the ocean surface layer provide insight into the process of air entrainment of breaking waves and allow the establishment of a well-defined breaking criterion, consistent with theoretical predictions. The lack of a single criterion for the detection of wave breaking might be one reason for the wide range of breaking frequencies given by different authors (cf. [Holthuijsen and Herbers 1986](#)). However, even if restricted to our measurements obtained with a single instrument and our use of a single breaking criterion, the fraction of breaking waves per dominant wave does not appear to scale with wind speed or wave age. It is generally accepted that wave breaking plays a significant role in energy dissipation in the oceanic surface layer and hence our results imply that energy dissipation cannot be determined solely from wind speed or wave age. Our analysis of breaking frequencies observed under a wide variety of fetch and wave age conditions suggests the energy transfer from the wind to the wave field as the driving parameter for breaking. Our datasets collapse to a roughly linear dependence when this energy transfer is combined with a breaking frequency normalized by the effective frequency of waves associated with dissipation of wave energy. This indicates that not only the flux of energy into the wave field but also the energy dissipation are strongly dependent on the high frequency tail of the wave spectrum and stresses the importance of accurate high frequency wave measurements. However, wave-wave interactions redistribute energy toward lower frequencies, and the importance of high frequency wave components in determining wave breaking does not imply that dissipation predominantly occurs at these short wave scales. Indeed, it was found that all wave scales larger than approximately one tenth of the dominant wavelength are associated with breaking and cause significant air entrainment. The median period of the observed breaking waves is 0.54 times the period of the dominant waves, comparing favorably with the very limited published results of other investigators. However the range of scales is much wider. Breaking waves are generally not the highest waves; their average wave height is  $\sim 70\%$  of the significant wave height. Presumably air entrainment occurs close to the wave crest, yet at 0.2-m depth the air is predominantly detected substantially downstream from the crest.

Air entrainment, detected at a single point, often reaches values of volumetric fractions  $>20\%$ . These high values, however, are restricted to the upper  $\sim 0.2$  m. In the open ocean  $\sim 2\%$  of breaking events show more deeply penetrating large air fractions, presumably associated with plunging, and 98% of deep water breaking waves have shallow air entrainment, characteristic for spilling type breaking waves. However, in two cases, namely a young wave field in a fetch limited coastal environment and under the condition of swell opposing wind waves, the occurrence of deeper penetrating air entrainment increased to 10% of the total number of breaking waves. Nevertheless, our data suggest that these deeper penetrating events, which are typical for plunging breakers, play a minor role in upper ocean dynamics.

### Acknowledgments

This work was made possible with the help of technical staff of the acoustical oceanography group at the Institute of Ocean Sciences, and with the support of the U.S. Office of Naval Research and the Canadian Natural Sciences and Engineering Council. We are indebted to the crews of RV *Parizeau*, RV *Tully*, and RV *Wecoma* for assistance in deployment and recovery of the instrumentation. Dr. Marsden provided the directional wave measurements for the 25 February 1992 deployment; Dr. J. Edson provided the meteorological data for 18 April 1995. We thank Drs. C. Garrett, R. Lueck, and J. Moum for helpful discussions and the reviewers for their constructive comments.

---

### REFERENCES

- Agrawal, Y. C., E. A. Terray, M. A. Donelan, P. A. Hwang, A. J. Williams III, W. M. Drennan, K. K. Kahma, and S. A. Kitaigorodskii, 1992: Enhanced dissipation of kinetic energy beneath surface waves. *Nature*, **359**, 219–220..
- Banner, M. L., 1990: Equilibrium spectra of wind waves. *J. Phys. Oceanogr.*, **20**, 966–984.. [Find this article online](#)
- Bortkovskii, R. S., 1987: *Air–Sea Exchange of Heat and Moisture during Storms*. D. Reidel, 194 pp..
- Cartwright, D. E., and M. S. Longuet-Higgins, 1956: The statistical distribution of the maxima of a random function. *Proc. Roy. Soc. London, Series A*, **137**, 212–232..
- Caudal, G., 1993: Self-consistency between wind stress, wave spectrum, and wind-induced wave growth for fully rough air–sea interface. *J. Geophys. Res.*, **98**, 22 743–22 752..
- Ding, L., and D. M. Farmer, 1994: Observations of breaking wave statistics. *J. Phys. Oceanogr.*, **24**, 1368–1387.. [Find this article online](#)
- Donelan, M., 1990: Air–sea interaction. *The Sea*. Vol. 9: *Ocean Engineering Sciences*, B. LeMehaute and D. M. Hanes, Eds., John Wiley and Sons, 239–292..
- , and W. J. Pierson, 1987: Radar scattering and equilibrium ranges in wind generated waves with applications to scatterometry. *J. Geophys. Res.*, **92**, 4971–5029..
- , J. Hamilton, and W. H. Hui, 1985: Directional spectra of wind generated waves. *Philos. Trans. Roy. Soc. London, Ser. A*, **315**, 509–562..
- Duncan, J. H., 1981: An investigation of breaking waves produced by a towed hydrofoil. *Proc. Roy. Soc. London, Series A*, **337**, 331–348..
- Farmer, D. M., and S. Vagle, 1988: On the determination of breaking surface wave distributions using ambient sound. *J. Geophys. Res.*, **93**, 3591–3600..
- , and J. R. Gemmrich, 1996: Measurements of temperature fluctuations in breaking surface waves. *J. Phys. Oceanogr.*, **26**, 816–825.. [Find this article online](#)
- , C. L. McNeil, and B. D. Johnson, 1993: Evidence for the importance of bubbles in increasing air–sea gas flux. *Nature*, **361**, 620–623..
- Gemmrich, J. R., 1997: A study of turbulence and fine scale temperature variability of the ocean thermal boundary layer under breaking surface waves. Ph.D. thesis, University of Victoria, 209 pp. [Available from University Microfilm, 300 N. Zeeb Rd., Ann Arbor, MI 48106.].
- , and D. M. Farmer, 1999: Near-surface turbulence and thermal structure in a wind-driven sea. *J. Phys. Oceanogr.*, **29**, 480–499.. [Find this article online](#)
- , T. D. Mudge, and V. D. Polonichko, 1994: On the energy input from wind to surface waves. *J. Phys. Oceanogr.*, **24**, 2413–2417..

Gower, J., and D. Jones, 1994: Canadian West Coast giant waves. *Mar. Wea. Log.* **38** (2), 4–8..

Hanson, J. L., 1996: Wind sea growth and swell evolution in the Gulf of Alaska. Ph.D. thesis, The Johns Hopkins University, 151 pp. [Available from University Microfilm, 300 Zeeb Rd., Ann Arbor, MI 48106..]

Holthuijsen, L. H., and T. H. C. Herbers, 1986: Statistics of breaking waves observed as whitecaps in the open sea. *J. Phys. Oceanogr.*, **16**, 290–297..

Hsiao, S. V., and O. H. Shemdin, 1983: Measurements of wind velocity and pressure with a wave follower during MARSSEN. *J. Geophys. Res.*, **88**, 9841–9849..

Jähne, B., 1991: New experimental results on the parameters influencing air–sea gas exchange. *Air–Water Mass Transfer*, ASCE, 582–592..

Jessup, A. T., C. J. Zappa, M. R. Loewen, and V. Hesany, 1997: Infrared remote sensing of breaking waves. *Nature*, **385**, 52–55..

Katsaros, K. B., and S. S. Ataturk, 1992: Dependence of wave-breaking statistics on wind stress and wave development. *Breaking Waves IUTAM Symposium*, M. L. Banner and R. H. J. Grimshaw, Eds., Springer-Verlag, 119–132..

Keeling, R. F., 1993: On the role of large bubbles in air–sea gas exchange and supersaturation in the ocean. *J. Mar. Res.*, **51**, 237–271..

Kinsman, B., 1965: *Wind Waves*. Prentice-Hall, 676 pp..

Kitaigorodskii, S. A., 1983: On the theory of the equilibrium range in the spectrum of wind-generated gravity waves. *J. Phys. Oceanogr.*, **13**, 816–827.. [Find this article online](#)

—, 1984: On the fluid dynamical theory of turbulent gas transfer across an air sea interface in the presence of breaking waves. *J. Phys. Oceanogr.*, **14**, 960–972.. [Find this article online](#)

Komen, G. J., L. Cavaleri, M. Donelan, K. Hasselmann, S. Hasselmann, and P. A. E. M. Janssen, 1994: *Dynamics and Modelling of Ocean Waves*. Cambridge University Press, 532 pp..

Lamarre, E., and W. K. Melville, 1992: Instrumentation for the measurement of void-fraction in breaking waves: Laboratory and field results. *IEEE J. Oceanic Eng.*, **17**, 204–215..

—, and —, 1994: Void-fraction measurements and sound-speed fields in bubble plumes generated by breaking waves. *J. Acoust. Soc. Amer.*, **95**, 1317–1328..

Ling, C. S., 1993: Effect of breaking waves on the transport of heat and vapor fluxes from the ocean. *J. Phys. Oceanogr.*, **23**, 2360–2372.. [Find this article online](#)

Longuet-Higgins, M. S., and J. S. Turner, 1974: An “entrainment plume” model of a spilling breaker. *J. Fluid Mech.*, **63**, 1–20..

—, and N. D. Smith, 1983: Measurement of breaking waves by a jump meter. *J. Geophys. Res.*, **88**, 9823–9831..

Melville, W. K., 1994: Energy dissipation by breaking waves. *J. Phys. Oceanogr.*, **24**, 2041–2049.. [Find this article online](#)

—, and R. J. Rapp, 1985: Momentum flux in breaking waves. *Nature*, **336**, 54–59..

Mitsuyasu, H., 1985: A note on the momentum transfer from wind to waves. *J. Geophys. Res.*, **90**, 3343–3345..

Monahan, E. C., and I. G. O’Muirheartaigh, 1986: Whitecaps and the passive remote sensing of the ocean surface. *Int. J. Remote Sens.*, **7**, 627–642..

Olsen, H. O., 1967: Theoretical and experimental investigation of impedance void meters. Ph.D thesis, University of Oslo, 141 pp. [Available from UNIK, Library, Granavn 33, Postboks 70, 2007 Kjeller, Norway..]

Phillips, O. M., 1985: Spectral and statistical properties of the equilibrium range of wind-generated gravity waves. *J. Fluid Mech.*, **156**, 505–531..

—, and M. L. Banner, 1974: Wave breaking in the presence of wind drift and swell. *J. Fluid Mech.*, **66**, 625–640..

Plant, W. J., 1982: A relationship between wind stress and wave slope. *J. Geophys. Res.*, **87**, 1961–1967..

Rapp, R. J., and W. K. Melville, 1990: Laboratory measurements of deep-water breaking waves. *Philos. Trans. Roy. Soc. London, Ser. A*, **331**, 731–800..

Skyner, D. J., and C. A. Greated, 1992: The evolution of a long-crested deep-water breaking wave. *Proc. Second (1992) Int. Offshore and Polar Engineering Conf.*, San Francisco, CA, ISOPE, 132–138..

Smith, S. D., 1981a: Factors for adjustment of wind speed over water to a 10-metre height. Bedford Institute of Oceanography Rep. Series/BI-R-81-3/March 1981, 29 pp..

— , 1981b: Coefficients for sea surface wind stress and heat exchange. Bedford Institute of Oceanography, Rep. Series/BI-R-81-19/December 1981, 31 pp..

Su, M.-Y., and J. Cartmill, 1992: Breaking waves statistics during ‘SWADE.’ *Breaking Waves IUTAM Symposium*, M. L. Banner and R. H. J. Grimshaw, Eds., Springer-Verlag, 161–164..

Terray E. A., M. A. Donelan, Y. C. Agrawal, W. M. Drennan, K. K. Kahma, A. J. Williams III, P. A. Hwang, and S. A. Kitaigorodskii, 1996: Estimates of kinetic energy dissipation under breaking waves. *J. Phys. Oceanogr.*, **26**, 792–807.. [Find this article online](#)

Thorpe, S. A., 1982: On the clouds of bubbles formed by breaking wind-waves in deep water, and their role in air–sea gas transfer. *Philos. Trans. Roy. Soc. London, Ser. A*, **304**, 155–210..

— , 1993: Energy loss by breaking waves. *J. Phys. Oceanogr.*, **23**, 2498–2502.. [Find this article online](#)

— , and P. N. Humphries, 1980: Bubbles and breaking waves. *Nature*, **283**, 463–465..

Toba, Y., H. Kunishi, K. Nishi, S. Kawai, Y. Shimada, and N. Shibata, 1971: Study on air–sea boundary processes at the Shirahama Oceanographic Tower Station (in Japanese with English abstract). Disaster Prevention Institute, Kyoto University Annals, Vol. 148, 519–531..

Trevorrow, M. V., and I. J. Booth, 1995: Extraction of ocean wave directional spectra using steerable Doppler side-scan sonars. *J. Atmos. Oceanic Technol.*, **12**, 1087–1100..

Weissman, M. A., S. S. Ataktürk, and K. B. Katsaros, 1984: Detection of breaking events in a wind-generated wave field. *J. Phys. Oceanogr.*, **14**, 1608–1619.. [Find this article online](#)

Woolf, D. K., and S. A. Thorpe, 1991: Bubbles and the air–sea exchange of gases in near saturation conditions. *J. Mar. Res.*, **49**, 435–466..

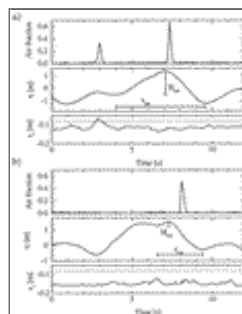
## Tables

Table 1. Summary of experimental conditions: wind direction (dd), wind speed ( $u_{10}$ ) corrected to 10-m height, significant wave height ( $H_s$ ), period of dominant wind waves ( $\tau_p$ ), and nominal depth of shallowest conductivity sensor  $z_y$ . Standard deviation  $\sigma$  are given for wind direction and wind speed.

Expt- no.	Date	Location	Fetch length (km)	dd (°)	$u_{10}$ (m s <sup>-1</sup> )	$H_s$ (m)	$\tau_p$ (s)	$z_y$ (m)	$\sigma_{dd}$	$\sigma_{u_{10}}$
I	24 Nov 1990	State of Georgia (30°45'N, 115°00'W)	20	90°	9.14	3-14	6-14	3-4.0	increasing 4.2-5.2	0.17
II	25 Feb 1992	Gulf of Alaska (60°40'N, 150°00'W)	unlimited	210-230 (then 400)	11.7-17.1	increasing 10-12	10-20	3-4.0	increasing 5.0	0.24
				210-230	11.7-17.1	10-12	10-20	3-4.0	increasing 5.0	0.24
III	3 Dec 1993	NE Pacific (40°37'N, 123°00'W)	80	330	7.0-8.1	increasing 4.0-6.0	4-6.0	4-4.0	increasing 0-10	0.18
IV	9 Dec 1993	NE Pacific (40°37'N, 123°00'W)	unlimited	330-300	12.0-10.0	increasing 12.0-20	12-20	4-4.0	increasing 0-12	0.19
V	18 Apr 1995	NE Pacific (40°37'N, 123°00'W)	unlimited	330	10.0-11.0	increasing 10-14	10-14	3-3.0	increasing 0-7	0.12

[Click on thumbnail for full-sized image.](#)

## Figures

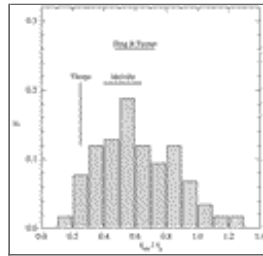


[Click on thumbnail for full-sized image.](#)

Fig. 1. Air fraction, surface elevation  $\eta$ , and sensor depth  $z_s$  below instantaneous surface during a breaking event. Height and

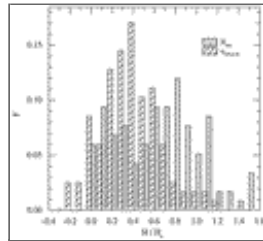


period of the breaking wave are indicated by  $H_{brk}$  and  $\tau_{brk}$  respectively. (a) 0150 PDT 18 Apr 1995; (b) 0221 PDT 18 Apr 1995.



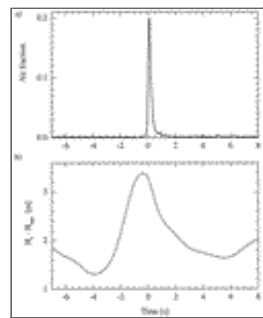
[Click on thumbnail for full-sized image.](#)

Fig. 2. Distribution of normalized period of breaking waves during deployment III. Bars refer to breaking scale estimates by [Thorpe \(1993\)](#), [Melville \(1994\)](#), and [Ding and Farmer \(1994\)](#).



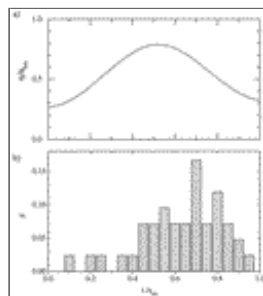
[Click on thumbnail for full-sized image.](#)

Fig. 3. Distribution of normalized height of breaking waves  $H_{brk}$  (gray) and normalized surface elevation at the onset of air entrainment  $\eta_{brk}$  (pattern) for deployment III.



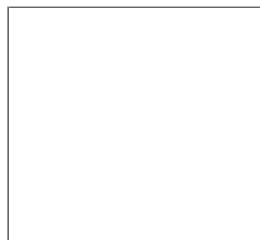
[Click on thumbnail for full-sized image.](#)

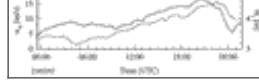
Fig. 4. Average breaking wave quantities during III: (a) air fraction at 0.18-m depth and (b) surface elevation above minimum elevation within the period of the breaking wave.



[Click on thumbnail for full-sized image.](#)

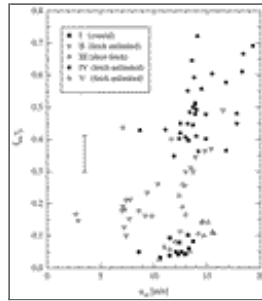
Fig. 5. (a) Average surface elevation of a breaking wave, normalized by wave height and wave period of each individual breaking wave. (b) Distribution of time of maximum air fraction. For deployment III.





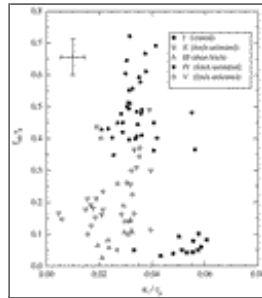
Click on thumbnail for full-sized image.

Fig. 6. Frequency of high air fraction due to wave breaking measured at different depths during deployment II. Applied air fraction thresholds are 0.08 at 0.24 m, 0.05 at 0.46 m, and 0.03 at 0.75 m. The instrument recorded only during odd hours and no data were collected between 1340 and 1520 UTC. Lower panel gives wind speed (solid) and significant wave height (dashes).



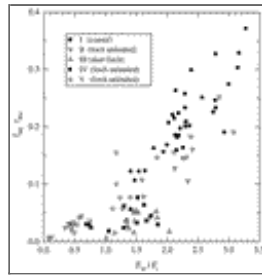
Click on thumbnail for full-sized image.

Fig. 7. Relative breaking frequency as function of wind speed for deployments I–V (see [Table 1](#)). Each data point represents a 30-min average. Error bar depicts mean of standard deviation for all averaging segments in III.



Click on thumbnail for full-sized image.

Fig. 8. Relative breaking frequency as function of inverse wave age. Same data points shown as in [Fig. 7](#). Vertical error bar represents mean of standard deviation for all averaging segments in III. Horizontal error bar is based on estimated uncertainties of  $u_*$  (40%) and  $c_p$  (20%).



Click on thumbnail for full-sized image.

Fig. 9. Normalized breaking frequency as function of scaled energy input into the wave field. Same data points shown as in [Fig. 8](#).

\* Current affiliation: Netherlands Institute for Sea Research, Den Burg, Texel, the Netherlands.

Corresponding author address: Dr. Johannes R. Gemmrich, Netherlands Institute for Sea Research, P.O. Box 59, 1790 AB Den Burg, Netherlands.

E-mail: [gemmrich@nioz.nl](mailto:gemmrich@nioz.nl)



© 2008 American Meteorological Society [Privacy Policy and Disclaimer](#)

Headquarters: 45 Beacon Street Boston, MA 02108-3693

DC Office: 1120 G Street, NW, Suite 800 Washington DC, 20005-3826

[amsinfo@ametsoc.org](mailto:amsinfo@ametsoc.org) Phone: 617-227-2425 Fax: 617-742-8718

[Allen Press, Inc.](#) assists in the online publication of *AMS* journals.